PAPER • OPEN ACCESS

Optical form measurement employing a tiltable line scanning, low coherence interferometer for annular subaperture stitching interferometry

To cite this article: Markus Schake *et al* 2021 *Meas. Sci. Technol.* **32** 105107

View the article online for updates and enhancements.

Optical form measurement employing a tiltable line scanning, low coherence interferometer for annular subaperture stitching interferometry

Markus Schake[1,*] , **Jörg Riebeling**[2,*] , **Peter Lehmann**[2] **and Gerd Ehret**[1]

[1] Physikalisch-Technische Bundesanstalt, Bundesallee 100, Braunschweig 38116, Germany
[2] Universität Kassel FB Elektrotechnik/Informatik, FG Messtechnik, Wilhelmshöher Allee 71, Kassel D-34121, Germany

E-mail: markus.schake@ptb.de and joerg.riebeling@uni-kassel.de

Abstract

This contribution presents experimental and simulation results of a tiltable line scanning low coherence interferometer applied for form measurement of spherical and aspherical objects with a diameter of up to 300 mm. The region of interest is sampled by multiple annular subapertures that are realigned employing stitching algorithms based on Cartesian- and Zernike polynomial fittings. The paper addresses common challenges in the reduction and modeling of displacement errors associated with the motion of the interferometric sensor between subaperture measurements and compares the topography deviations of the experimental results with those simulated by a Monte Carlo based model.

Keywords: interferometry, annular subaperture stitching, aspherical optics, form measurement, path length modulation, measurement uncertainty

(Some figures may appear in colour only in the online journal)

1. Introduction

The great potential and increasing application of aspherical lenses in precision optics and consumer products pushes research and development of contact free form measuring devices for quality control in industrial environments. Feasible form measurement devices shall meet industry's requirements in topography measurement precision, while providing a high dynamic measurement range to handle specimens of large diameter and variously sloped surface sections. Traceability of the measurement results to the national standard of length is required and an expanded uncertainty should be assigned to the measurement results for comparability.

Subaperture stitching interferometry (SSI) is a commonly used approach to combine axial and lateral resolution of an interferometer with a variable field of view [1–14]. SSI is a non-null test method, which does not require a fringe free interferogram generated by matching the reference wavefront to the specimen's topography. Thus, the cost and time intensive fabrication of digital holograms or null correctors is saved. Instead a planar wavefront of variable tilt or a spherical reference wavefront of variable radius is employed and compared with the topography of the local subapertures. If the field of view is adequately chosen, a resolvable fringe pattern will result for each subaperture in its local coordinate system, from which the local phase map is retrieved. Due to the interferometer's basic working principle, the retrieved

---

phase map does only contain information about the path length difference between the wavefront reflected from the specimen surface and the reference wavefront. Employing a tilted plane wave as reference removes the tilt information from each subaperture, while using a spherical reference wave additionally removes the local radius information of the subaperture [3]. If absolute form measurement is required, the lost information can be restored, applying precise knowledge of the reference wavefront form and its translational errors between subapertures, additional information from overlapping regions of subsequently measured subapertures or global optimization algorithms [9–11]. However, the restoration of the absolute specimen topography in global coordinates is challenging and usually the restored parameters of global tilt and radius are retrieved with a much higher uncertainty than the locally measured topography features of higher order.

For the measurement of spherical or aspherical rotationally symmetric specimens, the method of annular subaperture stitching interferometry (ASSI) was proposed [5]. Most of the devices employed for ASSI use spherical reference wavefronts and are implemented as areal measuring Fizeau [1–3, 6, 7, 14] or Twyman–Green [5, 13] interferometer configurations. An advantage of the spherical reference wavefront in comparison to the plane reference wave is the possibility to choose larger fields of view while maintaining resolvable fringes, since the radius of the local subaperture is compensated. The measurement results of a commercially available device combining ASSI with the stitching of multiple circular apertures are reported in [6, 7]. The references demonstrate the capability of the system to measure a 30 μm aspherical departure in a field of view with a diameter of $D = 50$ mm and other specimens with a clear aperture of up to $D = 200$ mm with root mean square (RMS) deviations in the low nm range and only 1 nm difference to the RMS value obtained with a null test. Another commercial device reported in [3] achieves similar results and measures on an aperture of $D = 70$ mm with an RMS deviation of 2 nm compared to the null test while handling departures of up to 1 mm to a best fit sphere (BFS). In [12, 13] a global fitting approach based on ASSI data is proposed for the subaperture stitching. The stitching algorithm employs information from consecutively overlapping areas and solves a global fitting problem to obtain the Zernike polynomial description of the translational errors between the subapertures to restore the global phase map. Comparing the results to a null test yields a peak to valley (PV) difference of $\Delta\text{PV} = 0.031\lambda$ and $\Delta\text{RMS} = 0.005\lambda$ [12], which results in a RMS deviation of ≈ 3 nm to the null test assuming $\lambda \approx 632$ nm. The complementary annular subaperture method is proposed in [1, 2] and employs a global model fitting using a set of low order Zernike coefficients to remove the translational errors between the subapertures while simultaneously fitting the global surface to a high order Zernike polynomial. Using a parabolic mirror with diameter $D = 130$ mm, f-number 2 and focal length $f = 2D$ as the specimen and removing piston, tilt, defocus and coma, the system measures $\text{PV} = 0.33\lambda$ and $\text{RMS} = 0.055\lambda$, which is in good agreement with the provided auto-collimation measurement for comparison. In summary, it may be stated that state of the art measurement devices based on ASSI are capable of measuring aspherical departures with a similar performance than null test configurations and a mayor source of deviations for ASSI devices are translational errors introduced during motion between the subapertures. However, for all the results presented above, a BFS and in some cases higher order Zernike corrections are subtracted from the measurement results, yielding no information about these form features.

Another approach employing SSI is given by the tilted-wave interferometer (TWI) [15]. The TWI employs a source array to illuminate the specimen from different angles simultaneously. The tilted wavefronts pass a transmission sphere and the resolvable fringe patterns associated with the respective sources are recorded separately on the detector. No movable parts are involved to switch between the subapertures. However, the system's retrace errors need to be calibrated, which is a complex procedure and the phase maps are retrieved by solving a complex inverse problem requiring a model of the specimen. Measurement results of the TWI provided in [15] measuring a steep asphere with an aspheric departure of 550 μm in the field of view of $D = 40$ mm show a PV deviation to the nominal shape of $\Delta\text{PV} = 1.5$ μm. The TWI is also used to measure the absolute radius of a multispherical freeform artifact with nominal radii $r_1 = 40$ mm, $r_2 = 39.5$ mm [16]. It measures the absolute radius with a deviation of $\Delta r_1 = 6.4$ μm and $\Delta r_2 = 5.6$ μm in comparison with the results of an interferometric radius bench [17] at Physikalisch-Technische Bundesanstalt, which is characterized by an expanded uncertainty of $U_r = 0.4$ μm for coverage factor $k_p = 2$ [18]. Another benchmark for measurement of aspherical surfaces is presented in [19] comparing multiple tactile and optical devices including coordinate measuring machines, ASSI setups and the TWI. Four different aspheres are measured by the devices and the BFS corrected results of each device are compared to a virtual reference topography. The average RMS deviations range from ≈ 1 to ≈ 30 nm and the average PV deviations are in the range of ≈ 10 to ≈ 400 nm with the methods performing quite differently in dependence of the specimen. The study also concluded, that the total measurement uncertainties including the spherical part would be expected higher.

This contribution demonstrates the application of a tiltable low coherence interferometer with a line-scan camera sensor and a plane reference wavefront for ASSI [4, 8–11, 20]. The employed Michelson interferometer features an actuated reference mirror and high precision scanning axis combining optical path length modulation for phase-shifting interferometry and unambiguous distance measuring in the local coordinate system by depth scanning white light interferometry. The application of a plane reference wavefront reduces the translational errors between subapertures to piston and tilt and enables the application of a modified stitching algorithm based on [1, 10, 11, 21], which combines a Cartesian polynomial fitting for the translational errors with a Zernike polynomial fitting for the global wavefront reconstruction in a global model fitting approach. The results of the global model fitting are compared to a cumulative stitching approach, retrieving the lost tilt information of the subapertures from the overlapping regions of adjacent rings. A virtual experiment based on
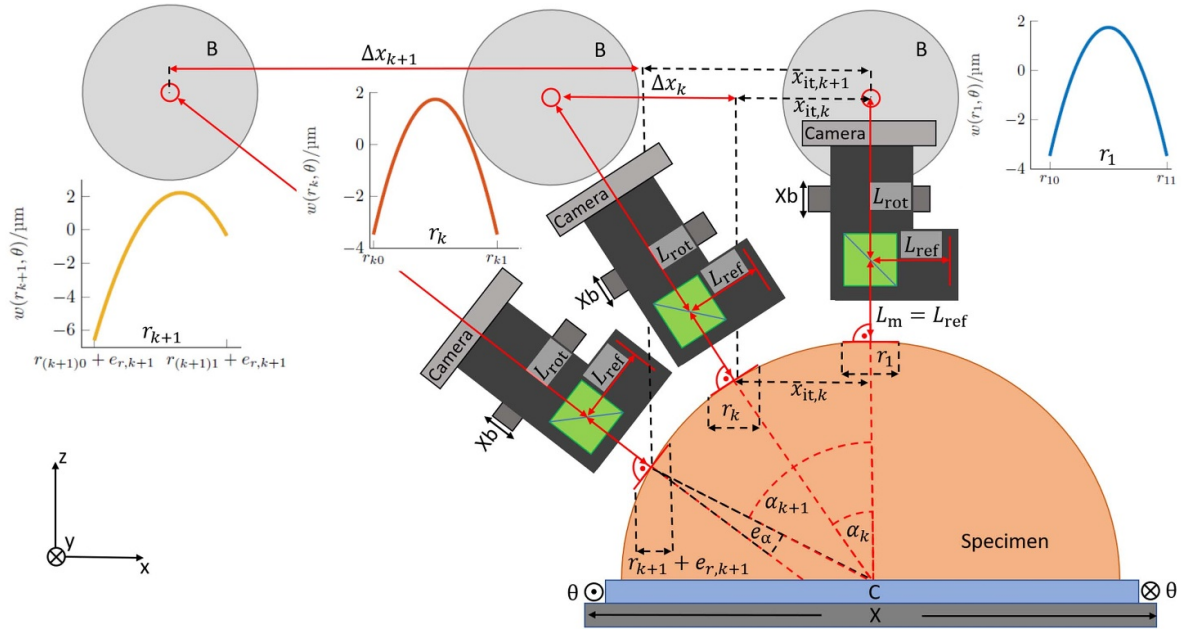
Figure 1. Schematic drawing of the Michelson interferometer facing different radial intervals r_k with x, y, z orientation of the global coordinate system, linear stage Xb, linear stage X, L_m distance to the specimen, L_{ref} distance to the reference plane, L_{rot} distance to the center of rotation of rotary stage B, Δx_k lateral displacement when tilting, α_k tilt angle, $x_{it,k}$ lateral displacement between subaperture measurements, r_{k0}, r_{k1} radial boundaries of the kth subaperture, θ azimuthal angle of rotary stage C, $e_{r,k}$ normally distributed radial displacement error based on the uncertainty $u_{r,k}$ (see equation (13)), e_α tilting error. For each interval r_k a section of the locally unwrapped topography $w(r_k, \theta)$ is depicted (blue-, red-, yellow line), the interferometer should always be aligned in the balanced path length distance $L_m = L_{ref}$.

[11] is proposed to model the influence of radial displacement errors on the modified topography stitching and to receive an estimate of the expanded measurement uncertainty. The virtual experiment is adapted to emulate the donut shaped locally unwrapped subapertures the interferometric topography measurement yields. It also considers the impact of the radial displacement errors on the retrieved radius, thus complying better to the experimental reality than the prior version employed in [11]. Experimental results of measurements at a $R = 150$ mm polished copper specimen and a mild glass asphere (asphere 1 [19]) are presented and compared to the simulation results. A fundamental difference between the presented setup and the ASSI setups described above is the planar reference wavefront. Due to this, the interferometer records the spherical departure to the reference plane for each subaperture and the global model fitting yields an estimate of the absolute radius, since defocus has not to be treated as a translational error. However, even for small fields of view, the spherical departure will be in the range of multiple mm, and is $10\times$ to $100\times$ larger than the aspherical departures usually considered, which causes a higher uncertainty in the radius retrieval compared to the parameters of the aspherical departure.

2. Experimental setup

The experimental setup consists of a Michelson interferometer with a line-scan camera detector and a four axis motion system to position the sensor relative to the specimen. A schematic drawing of the setup, showing the interferometric sensor

facing different radial intervals r_k and the associated locally unwrapped topography result $w(r_k, \theta)$, for an ideal spherical specimen, is depicted in figure 1. The light of a bandpass filtered green LED ($\lambda_{center} = 532$ nm, FWHM = 10 nm) is used as illumination. The light source is coupled into the interferometric probe head employing a liquid light guide to preclude influences of the LED's heat dissipation on the sensor. The Michelson interferometer uses a $5\times$-microscope objective with numerical aperture NA = 0.14. The interferometer's reference mirror is mounted on an oscillation coil, which is actuated with a frequency of 1 kHz during the annular subaperture measurement to cause a periodical optical path length modulation. The interferograms are recorded at a rate of 100 kHz by a line camera that comprises 4096 pixel. The oversampling of the path length modulated interference signals enables the application of noise robust, temporal carrier fringe based phase retrieval [11, 22] to retrieve the locally unwrapped topography $w(r_k, \theta)$ of each annular subaperture. The 2D-phase unwrapping of the local subaperture topographies is performed employing the algorithm proposed in [23]. Exemplary sections of the locally unwrapped topography $w(r_k, \theta)$ are depicted in figure 1 (blue-, red-, yellow line) for three different positions on an ideally spherical specimen. The specimen is mounted on the rotary stage C, rotating with the angle θ in azimuthal direction around the global z-axis to record the annular subapertures. Rotary stage C is mounted on the linear stage X, which is employed to compensate for the lateral displacement Δx_k when tilting the interferometer. The rotary stage B tilts the interferometer in the global x–z-plane with respect to the specimen. The linear stage Xb is mounted on

top of the rotary stage B and adjusts the distance of the interferometer perpendicular to the specimen surface to align it in the balanced path length condition $L_\mathrm{m} = L_\mathrm{ref}$. Details about the interferometric line sensor, its functions and applications as well as the motion system are reported in [4, 8, 20]. The absolute distance calibration to determine the length $L_\mathrm{m} + L_\mathrm{rot}$ as well as the details of the measurement procedure are reported in [9, 10]. The sequence of a topography measurement is shortly outlined below.

- The *X*-axis travels the distance $x_{\mathrm{it},k}$ to move the interferometer to the new radial interval r_k.
- The interferometer performs a depth scan [24] to align the probe in the balanced path length distance $L_\mathrm{m} = L_\mathrm{ref}$.
- Employing the topography information of the single camera line obtained from the depth scan, the local tilt of the sample with respect to the sensor is determined.
- The *B*-axis rotates to the angle α_k to compensate the local tilt and align the interferometer perpendicular to the specimen surface. The *X*-axis compensates the lateral displacement Δx_k caused by the titling procedure.
- Performing a second depth scan compensates the axial displacement associated with the rotation and restores the path length balance. The sensor should be positioned perpendicular to the specimen surface on the radial interval r_k as depicted in figure 1 (pos. 1, pos. *k*). If the interferometer is not aligned to the radial interval correctly and not perpendicular to the surface, radial and angular displacement errors $e_{r,k}, e_\alpha$ influence the topography result (see figure 1 pos. $k+1$).
- The specimen rotates in azimuthal direction by the angle θ. During rotation the reference arm is actuated and the carrier fringe based phase retrieval is employed to measure the topography of the annular subaperture.

The measurement sequence is repeated *K*-times until the entire topography of the specimen is sampled into *K* locally unwrapped annular subapertures $w(r_k, \theta)$. From these annular subapertures the global topography is restored employing stitching algorithms.

3. Topography stitching

During measurement the topography is recorded as multiple overlapping subapertures. Since the interferometer is tilted with respect to the sample between measurements, the global slope information of the annular subapertures is lost and the topography is measured as the deviation of the local subaperture to the plane reference wavefront. Thus, the retrieved locally unwrapped topographies $w(r, \theta)$ of the subapertures show a donut like shape as depicted in figures 1 and 2(a). Each subaperture is defined in a local coordinate system $r \in r_k = [r_{k0}, r_{k1}]$. However, each point on the topography, which is represented by the global wavefront $W(r, \theta)$ or the locally unwrapped wavefront $w(r, \theta)$, is assigned an unambiguous set of lateral coordinates (r, θ), in the global coordinate system, with *r* indicating the radius and θ accounting for the azimuthal angle. The global lateral coordinates are

assigned based on the current position of the *C*, *X*, *Xb* and *B*-axis and the calibrated absolute distance $L_\mathrm{ref} + L_\mathrm{rot}$ between the center of rotation of the *B*-axis and the specimen if the interferometer is positioned in the balanced path length distance $L_m = L_\mathrm{ref}$ with respect to the surface. The first subaperture on the interval r_1 shows greater height difference than the other subapertures, because for the first measurement the interferometer is positioned perpendicular to the global pole of the specimen, that is located at the border of the field of view. This first subaperture is employed as the basis for the cumulative stitching procedure. For the other subapertures the interferometer is tilted to compensate the global slope of the topography within the field of view. Since the curvature of a spherical object is constant, the height elevation of the $k > 1$ subapertures is also constant. Details concerning the calibration procedure and the determination of the radial position's standard uncertainty $u_{r,k}$ are reported in [9, 11]. To retrieve the global topography $W(r, \theta)$, a cumulative and a global stitching algorithm are employed. The cumulative stitching algorithm is based on the algorithm reported in [9, 11, 21] and the global stitching algorithm is based on [1, 9–13, 21]. The stitching algorithms are adapted to be capable of handling the locally unwrapped topography sections $w(r_k, \theta)$ depicted in figure 2(a). In [9–11] the annular subapertures were considered to be globally unwrapped, the tilt of the adjacent subapertures would match in the overlapping areas and the translational errors between two subapertures could be fitted into a low order $M = 3$ Zernike coefficient polynomial. However, due to the tilting of the interferometer, the global slope information of the subapertures is lost. As depicted in figure 2(a) the slope of the subapertures in the overlapping regions does not match. If the difference between two subapertures in the overlapping regions is considered in cartesian coordinates, it is expressed as a closed ring with a height gradient in radial direction as depicted in the upper part of figure 2(b). This form contains Zernike coefficients of higher order and may not be compensated by a polynomial fit employing $M = 3$ Zernike coefficients. Thus, the stitching procedure applied in [9–11] can not be used with the locally unwrapped topography. However, transforming the difference in the overlapping area into polar coordinates, results in the unfolding of the ring into a plane as depicted in the lower part of figure 2(b).

3.1. Cumulative stitching

Considering the first subaperture on the interval r_1 as the basis subaperture, the lost tilt information of the overlapping aperture in the interval r_2 may be retrieved as the gradient of the plane in radial direction. Thus, the offset and tilt of the plane are fitted in a cartesian polynomial of first order

$$f(r_k \cap r_{k+1}) = m_{r_k \cap r_{k+1}} \cdot (r_k \cap r_{k+1}) + b \qquad (1)$$

and extrapolated to the whole subaperture r_2 to restore the global tilt information. Since the tilt difference between the base subaperture r_k and the adjacent subaperture r_{k+1} is described by the linear function in equation (1), the extrapolation to the subaperture interval r_{k+1} which should be aligned
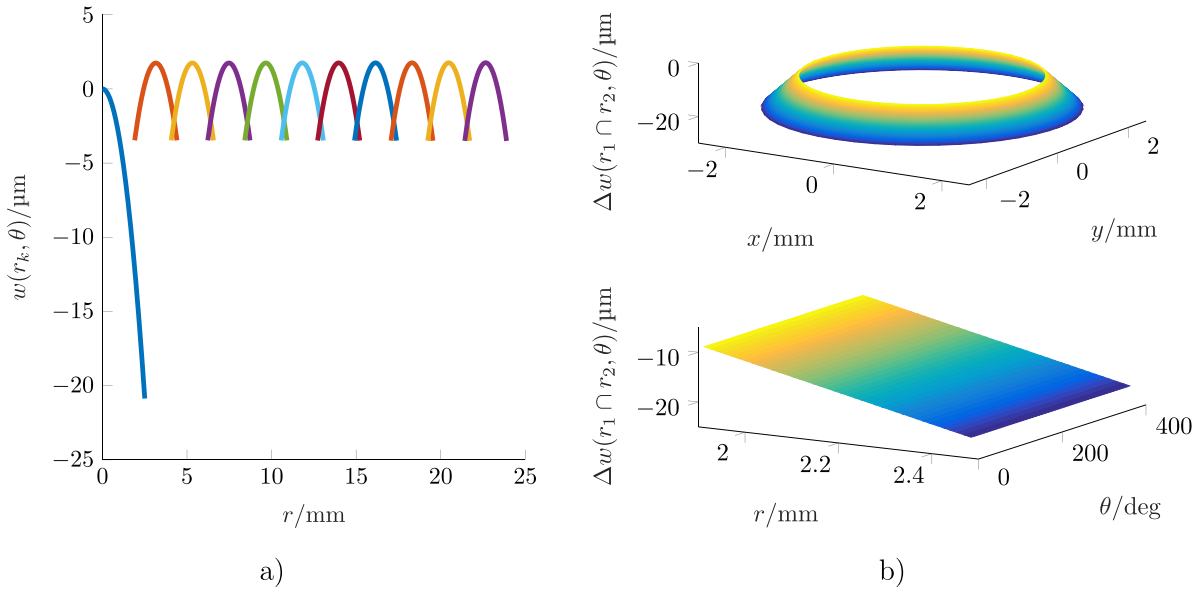
Figure 2. (a) Sectional view of the simulated locally unwrapped topography of a sphere with radius of curvature $R = 150$ mm and specimen diameter $D = 50$ mm, sampled in $K = 11$ overlapping subapertures. (b) Topography difference in the overlapping region $r_k \cap r_{k+1}$ of subapertures $k = 1, 2$ depicted as a closed ring in Cartesian coordinates and a plane in polar coordinates.

to r_k is simply performed by using $m_{r_{k+1}} = m_{r_k \cap r_{k+1}}$ and adding a plane with the linear height elevation in equation (2) in radial direction to the local wavefront $w(r_{k+1}, \theta)$.

$$f(r_{k+1}) = m_{r_{k+1}} \cdot r_{k+1} + b \tag{2}$$

$$W(r_{k+1}, \theta) = w(r_{k+1}, \theta) + f(r_{k+1}). \tag{3}$$

The global wavefront $W(r, \theta)$ is restored in an iterative process $k \in [1, \ldots, K]$, starting from the base subaperture assuming $W(r_1, \theta) = w(r_1, \theta)$ and applying equations (1)–(3) to restore the tilt information of the adjacent subapertures from their difference in the overlapping region. In this process the restored tilt and offset information is accumulating since the last part of the global wavefront would be calculated as

$$W(r_K, \theta) = w(r_K, \theta) + \sum_{k=1}^{K-1} f(r_{k+1}). \tag{4}$$

The cumulative stitching progress is illustrated in figure 3(a). The radius r is normalized to the diameter D. The global wavefront $W(r_k, \theta)$, which still consists of discrete subapertures, may be fitted into a Zernike polynomial with $L = 36$ coefficients. This yields a continuous description

$$W_{\mathrm{cum}}(r, \theta) = X \cdot P_{\mathrm{cum}} \tag{5}$$

of the topography [11]. Thereby, $[X]_{N_{\mathrm{glo}} \times L}$ contains the Zernike polynomials evaluated at the N_{glo} sample points totally included in all subapertures in the global coordinate system and $[P_{\mathrm{cum}}]_{L \times 1}$ contains the Zernike coefficients retrieved by fitting the point cloud $W(r_k, \theta) \forall k = 1, \ldots, K$ to the Zernike polynomials employing the optimization problem described in [10, 21]. The first three Zernike coefficients of piston and tilt

in the matrix P_{cum} may be ignored, since they solely depend on the parameters of the subaperture chosen as the basis for the cumulative stitching and may not be unambiguously retrieved from the recorded interferograms.

3.2. Global stitching

The global stitching algorithm is based on the stitching procedure applied in [10, 11] but evolved to handle the locally unwrapped subapertures $w(r_k, \theta)$. In previous applications of the global stitching algorithm, the translational errors between the subapertures were fitted into the $M = 3$ Zernike polynomials of piston and tilt, while the global wavefront was retrieved in terms of the $L - M$ higher order Zernike coefficients. However, the translational errors between the locally unwrapped subapertures can not be described in terms of a $M = 3$ coefficient Zernike polynomial, but are handled by a linear fit in polar coordinates, as outlined in the last section considering the cumulative stitching. Therefore, the global stitching problem is formulated in equation (7) applying cartesian polynomials $C_{ki}(r_k, k)$ with $M = 2$ coefficients to describe the offset and tilt difference between the subapertures in radial direction and the $L - 3$ Zernike coefficients $Z_{ki}(r_k, \theta, k)$ of higher order to describe the stitched global wavefront. The first three Zernike coefficients of piston and two tilts are still omitted in the global wavefront fitting, since the orientation of the retrieved wavefront in these terms is not unambiguously defined by the interferometric input data. Similar to the cumulative stitching, the Cartesian polynomials are only employed to model the tilt of the kth subaperture in radial direction. This precludes the introduction of a tilt in the azimuthal direction, which would break the ring shaped subaperture open. Similar to equation (2), the Cartesian polynomials for $M = 2$ take the form
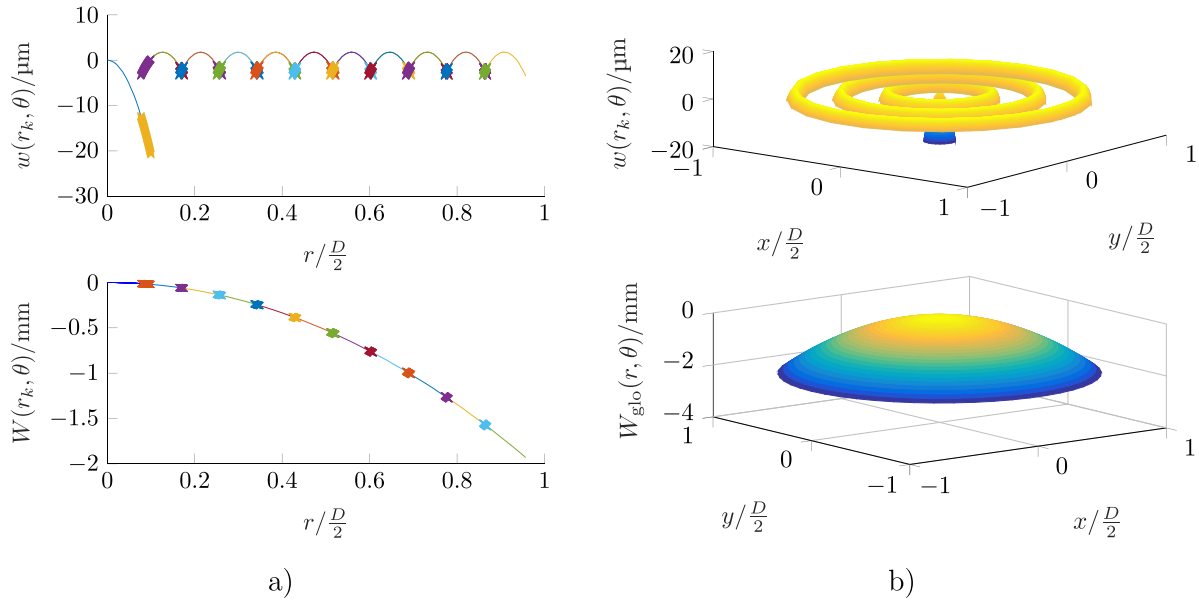
Figure 3. (a) Sectional view of the simulated locally unwrapped topography $w(r_k, \theta)$ of a sphere with radius of curvature $R = 150$ mm and specimen diameter $D = 50$ mm, sampled in $K = 11$ overlapping subapertures with marked overlapping regions and the restored global wavefront $W(r_k, \theta)$ after cumulative stitching. (b) Areal view of the simulated locally unwrapped topography $w(r_k, \theta)$, sampled in $K = 4$ not overlapping subapertures and the restored global wavefront $W_{\text{glo}}(r, \theta)$ after global stitching.

$$\sum_{i=1}^{2} b_{ki} C_{ki}(r_k, k) = b_{k2} r_k + b_{k1}. \qquad (6)$$

In equation (6), the coefficients b_{ki} account for the local piston and tilt of each subaperture. The global stitching problem is formulated as

$$\underbrace{w(r, \theta)}_{Y} = \underbrace{\sum_{k=1}^{K} \left[\sum_{i=1}^{M} b_{ki} C_{ki}(r_k, k) + \sum_{i=4}^{L} B_i Z_{ki}(r_k, \theta, k) \right]}_{\tilde{X} \cdot \tilde{P}}. \qquad (7)$$

In equation (7) the locally unwrapped global wavefront $w(r, \theta) = [Y]_{KN_{\text{sub}} \times 1}$ represents the point cloud of the sampled surface topography with N_{sub} sample points on each of the K subapertures. The matrix representation of the Cartesian and Zernike polynomials evaluated at the supporting points represented by $[\tilde{X}]_{KN_{\text{sub}} \times (KM + (L-3))}$ and $[\tilde{P}]_{(KM + (L-3)) \times 1}$ refers to the vector of the unknown local, b_{ki} cartesian and global B_i Zernike coefficients. As pointed out in [10], this can be formulated as a compact matrix equation

$$\underbrace{\begin{bmatrix} \vec{Y}_1 \\ \vdots \\ \vec{Y}_k \\ \vdots \\ \vec{Y}_K \end{bmatrix}}_{Y} = \underbrace{\begin{bmatrix} C_{b1} & 0 & \cdots & 0 & Z_{B1} \\ 0 & \ddots & & \vdots & \vdots \\ \vdots & & \ddots & 0 & \vdots \\ 0 & 0 & 0 & C_{bK} & Z_{BK} \end{bmatrix}}_{\tilde{X}} \underbrace{\begin{bmatrix} \vec{b}_1 \\ \vdots \\ \vec{b}_K \\ \vec{B} \end{bmatrix}}_{\tilde{P}}. \qquad (8)$$

The $\vec{Y}_k$ vectors each contain the point cloud of the N_{sub} sample points on the kth subaperture, $[C_{bk}]_{N_{\text{sub}} \times M}$ and $[Z_{Bk}]_{N_{\text{sub}} \times (L-3)}$ are the Cartesian and Zernike polynomials of the local and

global coefficients evaluated for (r_k, θ) of the respective kth subaperture. The Cartesian coefficient vector $\vec{b}_k$ and Zernike coefficient vector $\vec{B}$ are of dimension $M \times 1$ and $(L - 3 \times 1)$ respectively. The vector of the desired coefficients $\tilde{P}$ results immediately from the solution of the least squares problem [10, 21]

$$\tilde{P} = \left(\tilde{X}^T \tilde{X} \right)^{-1} \cdot \tilde{X}^T Y. \qquad (9)$$

Considering the setup of the matrix $\tilde{X}$ and the coefficient vector $\tilde{P}$, the optimization problem may be verbalized as follows:

Find the Zernike polynomial fit employing the polynomials of index $i = 4, \ldots, L$, which considering the least square criterion optimally fits into the point cloud of the locally unwrapped input topography $w(r, \theta)$ after adding an arbitrary offset and tilt to each of the subapertures.

Due to the continuity of the Zernike polynomials, the adjacent subapertures are stitched to each other by adapting their offsets and tilts. Compared to the cumulative stitching the global method does not require any overlap between the subapertures and the whole optimization problem is calculated in a single step. Thus, fitting aberrations do not accumulate. An exemplary result of the global stitching is provided in figure 3(b). To enable comparison of the cumulative and global stitching procedure the parameter vector $[P_{\text{glo}}]_{L \times 1}$ describing the Zernike polynomial fit of the global wavefront $W(r, \theta)$ is extracted from the extended parameter vector $\tilde{P}$. This is done by copying the last $L - 3$ coefficients of $\tilde{P}$ and replacing the first three coefficients with zeros:

$$P_{\text{glo}} = [0, 0, 0, \tilde{P}(KM + 1, \ldots, KM + L - 3)^T]^T.$$

Then the globally stitched wavefront $W_{\text{glo}}(r,\theta)$ results in

$$W_{\text{glo}}(r,\theta) = \boldsymbol{X} \cdot \boldsymbol{P}_{\text{glo}}. \tag{10}$$

Thereby, $[\boldsymbol{X}]_{N_{\text{glo}} \times L}$ includes the Zernike polynomials evaluated at the N_{glo} sample points totally covered by all subapertures in the global coordinate system analog to equation (5).

4. Modeling the expanded uncertainty by virtual experiments

Performing a topography measurement with the annular subaperture stitching interferometer yields the global wavefront $W(r,\theta)$ describing the specimens topography as the result of the cumulative $W_{\text{cum}}(r,\theta)$ or global $W_{\text{glo}}(r,\theta)$ stitching. The retrieved global wavefronts $W_{\text{cum}}(r,\theta)$, $W_{\text{glo}}(r,\theta)$ are estimates of the true unknown measurand $\tilde{W}(r,\theta)$. To obtain comparable topography results, the topography estimate $W(r,\theta)$ needs to be assigned a statement of expanded uncertainty [11, 25]

$$U_W = k_p u_W. \tag{11}$$

The expanded uncertainty U_W defines a confidence interval with a specific coverage probability p, which is referred to as coverage interval [25]

$$W(r,\theta) - U_W \leqslant \tilde{W}(r,\theta) \leqslant W(r,\theta) + U_W. \tag{12}$$

The expanded uncertainty U_W depends on the combined uncertainty u_W and the coverage factor k_p as given in equation (11). To obtain the coverage factor k_p the probability distribution of the measurement results $W(r,\theta)$ with the combined uncertainty u_W is required. The combined uncertainty u_W is estimated employing the experimental standard deviation of the topographies retrieved by the virtual experiments and the coverage factor is chosen based on the probability distribution of the results. Details about the virtual experiment, the underlying Monte Carlo simulation, the modeled deviations and their probability distribution are reported in [11]. However, the setup of the virtual experiment and the important input parameters are summarized here shortly. A main source

of topography deviations are lateral displacement errors occurring during the transition between subaperture measurements. Between consecutive subaperture measurements the interferometer is moved to a new lateral position, tilted by the B rotary stage and the X and Xb stage have to be moved accordingly to maintain the field of view centered on the radial interval $r_k = [r_{k0}, r_{k1}]$. In this process each of the mechanical stages contributes a positioning uncertainty. The calibrated absolute distance $L_{\text{ref}} + L_{\text{rot}}$ between the center of rotation of the B stage and the specimen with the interferometer positioned in the balanced path length distance $L_m = L_{\text{ref}}$ also contributes the uncertainty u_L. This uncertainty u_L of the absolute distance to the center of rotation translates into a lateral displacement uncertainty $u_{x,c}$ when tilting the interferometer. These positioning uncertainties accumulate into the combined radial displacement uncertainty $u_{r,k}$, which specifies the expected position uncertainty of the radial interval on the kth subaperture $r_k + u_{r,k} = [r_{k0}, r_{k1}] + u_{r,k}$. A statistical error in the interval width is currently not included in the model. The experiment for the estimation of u_L and the detailed derivation of $u_{r,k}$ are reported in [11]. The lateral displacement errors mentioned above may also be interpreted as wavefront deformations of the incoming global wavefront in the measurement path, retrieved by aligning the respective incoming wavefronts of each subaperture along the motion trajectory of the interferometer. This is useful to explain systematic topography deviations, which are not covered by the expanded uncertainty and will be discussed later. In [11] a model is proposed to obtain an estimate of the radial uncertainty $u_{r,k}$ in dependence of the X stage's uncertainties $u_{x,\text{it}} \approx 1$ µm, the B rotation stage uncertainty $u_\alpha \approx 1''$, the calibrated lateral position uncertainty when tilting the B-axis $u_{x,c} \approx 0.35$ µm, the calibration angle $\alpha_c = 1°$, the current tilt angle on the kth subaperture α_k and the width of the field of view when oriented perpendicular to the x-axis $|r_{k1} - r_{k0}|_\perp$. The model proposed in [11] is adapted by employing the same $u_{x,\text{it}}$ for all subapertures and adding the uncertainty $(L_{\text{ref}} + L_{\text{rot}}) \cdot u_\alpha$, which accounts for the immediate influence of the tilting error e_α (figure 1 pos. $k+1$) on the radial position error. The absolute distance $(L_{\text{ref}} + L_{\text{rot}})$ to the center of rotation of the B-axis is retrieved as a result of the calibration. This results in the expression

$$u_{r,k} = \sqrt{\left((L_{\text{ref}} + L_{\text{rot}}) \cdot u_\alpha\right)^2 + (u_{x,\text{it}})^2 + \left(\frac{\tan(\alpha_k)}{\tan(\alpha_c)} \cdot u_{x,c}\right)^2 + \left(\frac{1}{2}\left(|r_{k1} - r_{k0}|_\perp \sin(\alpha_k)\right) \cdot u_\alpha\right)^2} \tag{13}$$

for the radial displacement uncertainty. To yield proper results employing equation (13), the uncertainty u_α needs to be provided in radiants. The uncertainties $u_{x,\text{it}}$, u_α and $u_{x,c}$ belong to normally distributed errors and thus, radial displacement errors $e_{r,k}$ are modeled normally distributed with the standard deviation $u_{r,k}$. In the virtual experiment the normally

distributed radial displacement errors $e_{r,k}$ are applied to the sampling of the simulated measurand $\tilde{W}(r,\theta)$ and propagate through the stitching procedures to the retrieved topography estimate $W(r,\theta)$, from which the combined uncertainty u_W and the probability distribution of the topography are retrieved. The simulated results are compared to measurement results,
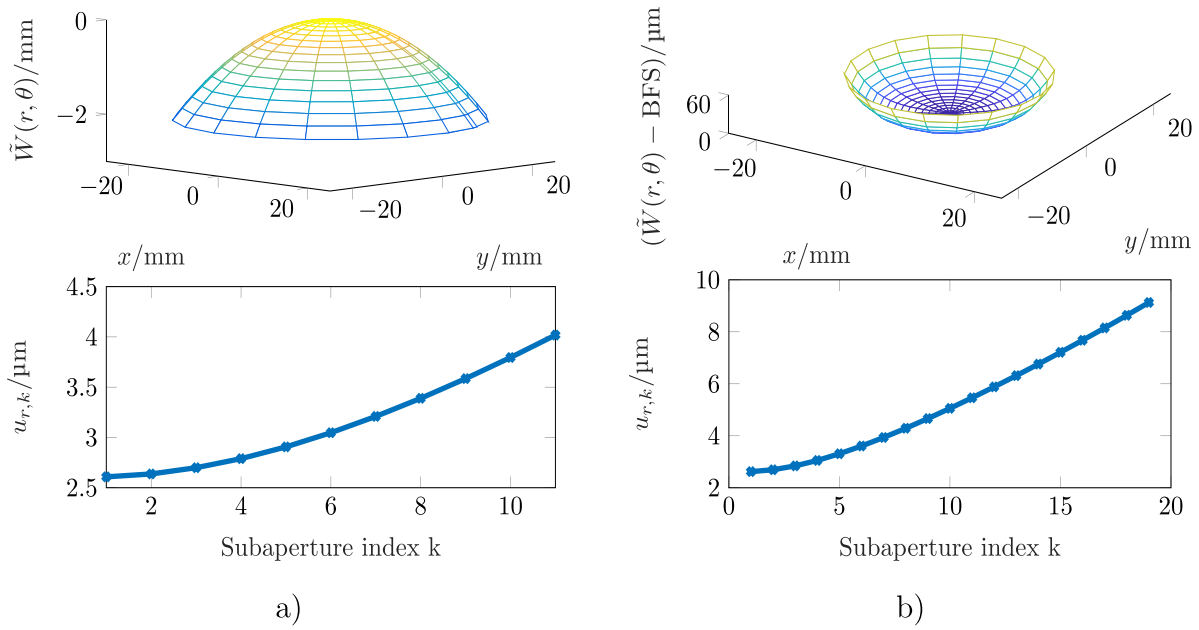
Figure 4. (a) Sphere, with a radius of curvature $R_{\mathrm{sph}} = 150$ mm employed in the virtual experiment and the associated radial uncertainty $u_{r,k}$ employed to simulate the normally distributed radial displacement errors on each subaperture. (b) Aspherical part of the employed aspherical specimen after subtracting a BFS with $R_{\mathrm{asph}} = 40.6193$ mm and the associated radial uncertainty $u_{r,k}$ employed to simulate the normally distributed radial displacement errors on each subaperture.

to check the plausibility of the combined uncertainty u_W and the expanded uncertainty U_W retrieved from the virtual experiment. The design function of two specimens, which are measured in the experiment, is employed in the virtual experiment.

- The first specimen is a diamond turned copper sphere, with a radius of curvature of $R_{\mathrm{sph}} = 150$ mm. The width of the field of view on a single subaperture when oriented perpendicular to the x-axis is $|r_{k1} - r_{k0}|_{\perp} = 2.5$ mm. In the virtual experiment $K = 11$ subapertures are simulated covering a total field of view of $D_{\mathrm{FOV}} \approx 47.731$ mm of the specimen diameter $D = 50$ mm. The specimen and the subaperture dependent development of $u_{r,k}$ are depicted in figure 4(a).
- The second specimen is a weak asphere [19] with a radius of curvature $R_{\mathrm{asph}} = 40.6193$ mm and the higher aspherical components
  - $A4 = -6.79375 \times 10^{(-7)}$ mm^{-3}
  - $A6 = -4.85203 \times 10^{(-10)}$ mm^{-5}
  - $A8 = -2.05223 \times 10^{(-13)}$ mm^{-7}
  - $A10 = -6.2324 \times 10^{(-17)}$ mm^{-9}
  - $A12 = -4.4857 \times 10^{(-20)}$ mm^{-11}.
- The width of the field of view on a single subaperture when oriented perpendicular to the x-axis is $|r_{k1} - r_{k0}|_{\perp} = 1.25$ mm. In the virtual experiment $K = 19$ subapertures are simulated covering a total field of view of $D_{\mathrm{FOV}} \approx 34.7$ mm of the specimen diameter $D = 35$ mm. The aspherical part of the specimen and the subaperture dependent development of $u_{r,k}$ are depicted in figure 4(b).

The Zernike polynomial fitting proposed in [10, 21] is employed to fit the fiducial measurand $\tilde{W}(r,\theta)$ of

each specimen into a $L = 36$ Zernike coefficient polynomial $[\boldsymbol{P}_{\mathrm{inp}}]_{L \times 1}$, which describes the fiducial topography on the unit circle $[\boldsymbol{X}]_{N_{\mathrm{glo}} \times L}$, with a small fitting error $|\tilde{W}(r,\theta) - \boldsymbol{X} \cdot \boldsymbol{P}_{\mathrm{inp}}| < 10$ nm. The virtual experiment is employed to generate $N = 10\,000$ topography samples considering the normally distributed radial displacement uncertainty $u_{r,k}$. This yields a set of $N = 10\,000$ output topographies, each described by the Zernike polynomial vectors $[\boldsymbol{P}_{\mathrm{cum}}]_{L \times 1}$ for the cumulative and $[\boldsymbol{P}_{\mathrm{glo}}]_{L \times 1}$ for the global stitching procedure. The mean value of the output polynomials $\vec{\mu}_{\boldsymbol{P}_{\mathrm{cum}}}, \vec{\mu}_{\boldsymbol{P}_{\mathrm{glo}}}$ is compared to $\boldsymbol{P}_{\mathrm{inp}}$ to identify systematic errors associated with the stitching procedures and the standard deviation of the output vectors $\vec{u}_{\boldsymbol{P}_{\mathrm{cum}}}, \vec{u}_{\boldsymbol{P}_{\mathrm{glob}}}$ is employed to estimate the combined and expanded uncertainty [11]

$$
\begin{aligned}
u_{W,\mathrm{glo}} &\approx \boldsymbol{X} \cdot \vec{u}_{\boldsymbol{P}_{\mathrm{glo}}} \\
U_{W,\mathrm{glo}} &\approx k_p \boldsymbol{X} \cdot \vec{u}_{\boldsymbol{P}_{\mathrm{glo}}}.
\end{aligned}
\tag{14}
$$

In equation (14) $[\boldsymbol{X}]_{N_{\mathrm{glo}} \times L}$ contains the Zernike polynomial values of L Zernike polynomials evaluated at N_{glo} points on the unit circle. Multiplication of $\boldsymbol{X}$ with the Zernike coefficient vectors $\boldsymbol{P}_{\mathrm{glo}}$ or $\boldsymbol{P}_{\mathrm{cum}}$ would yield the surface form as described by the Zernike polynomials. Multiplying it with the uncertainty of the Zernike coefficient vectors $\vec{u}_{\boldsymbol{P}_{\mathrm{glo}}}$ or $\vec{u}_{\boldsymbol{P}_{\mathrm{cum}}}$ yields the combined uncertainty of the surface form instead, which describes the normally distributed statistical deviations caused by the normally distributed radial displacement errors and other statistical aberrations. The combined uncertainty is multiplied with the coverage factor k_p to receive the expanded uncertainty. In case of the normal distribution, k_p is associated with a $k_p \sigma$ coverage interval with σ referring to the variance
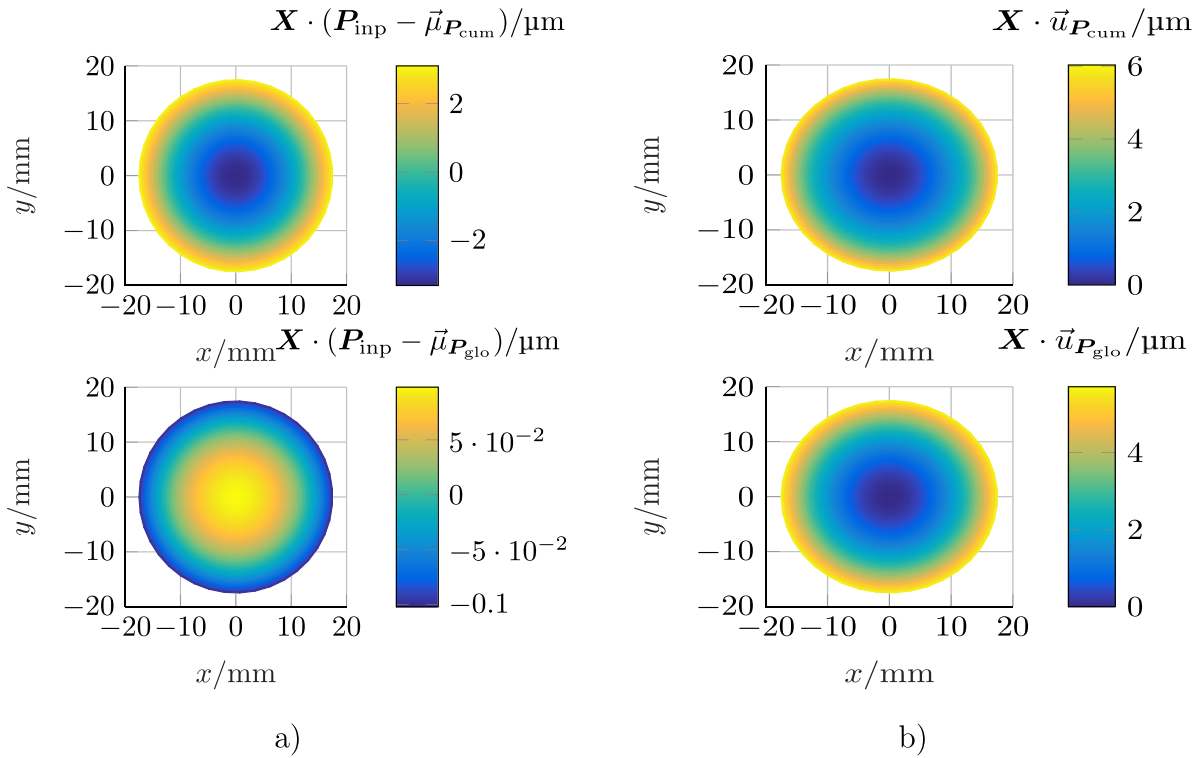
Figure 5. Aspherical specimen ($K = 19$, $\alpha_K \approx 23.6°$): (a) difference between the mean value of the retrieved output topographies, described by the Zernike coefficient vectors as given in equations (5) and (10), and the fiducial input topography represented by the coefficients of $\boldsymbol{P}_{\text{inp}}$. This difference indicates systematic errors in the stitching procedures. (b) Estimates of the combined uncertainty $u_{W,\text{cum}}$ and $u_{W,\text{glo}}$ as defined in equation (14) in dependence of the lateral position in the field of view.

Table 1. Aspherical specimen ($K = 19$, $\alpha_K \approx 23.6°$): difference of the mean value of the output polynomials $\vec{\mu}_{\boldsymbol{P}_{\text{cum}}}$, $\vec{\mu}_{\boldsymbol{P}_{\text{glo}}}$ and the fiducial input $\boldsymbol{P}_{\text{inp}}$. Standard deviation of the Zernike coefficient vectors $\vec{u}_{\boldsymbol{P}_{\text{cum}}}$ and $\vec{u}_{\boldsymbol{P}_{\text{glo}}}$ as visualized in figure 5. The coefficients i are selected to show the main contributing coefficients $i = 5, 13, 25$ and their neighboring coefficients for comparison.

i	$(\boldsymbol{P}_{\text{inp}} - \vec{\mu}_{\boldsymbol{P}_{\text{cum}}})/\mu\text{m}$	$(\boldsymbol{P}_{\text{inp}} - \vec{\mu}_{\boldsymbol{P}_{\text{glo}}})/\mu\text{m}$	$\vec{u}_{\boldsymbol{P}_{\text{cum}}}/\mu\text{m}$	$\vec{u}_{\boldsymbol{P}_{\text{glo}}}/\mu\text{m}$
4	7.67×10^{-06}	3.03×10^{-08}	1.34×10^{-05}	5.77×10^{-10}
5	3.23	-0.10	2.88	2.86
6	1.85×10^{-05}	7.32×10^{-08}	3.23×10^{-05}	1.39×10^{-09}
12	1.33×10^{-05}	4.22×10^{-09}	2.22×10^{-05}	3.05×10^{-10}
13	-0.11	-0.18×10^{-02}	0.19	0.06
14	3.22×10^{-05}	1.02×10^{-08}	5.36×10^{-05}	7.37×10^{-10}
24	9.57×10^{-05}	7.17×10^{-09}	0.02×10^{-02}	3.36×10^{-08}
25	-0.02	-1.73×10^{-05}	0.13	0.06×10^{-02}
26	0.02×10^{-02}	1.73×10^{-08}	0.04×10^{-02}	8.12×10^{-08}

Table 2. Spherical specimen ($K = 11$, $\alpha_K \approx 8.7°$): difference of the mean value of the output polynomials $\vec{\mu}_{\boldsymbol{P}_{\text{cum}}}$, $\vec{\mu}_{\boldsymbol{P}_{\text{glo}}}$ and the fiducial input $\boldsymbol{P}_{\text{inp}}$. Standard deviation of the Zernike coefficient vectors $\vec{u}_{\boldsymbol{P}_{\text{cum}}}$ and $\vec{u}_{\boldsymbol{P}_{\text{glo}}}$. The coefficients i are selected to show the main contributing coefficients $i = 5, 13, 25$ and their neighboring coefficients for comparison.

i	$(\boldsymbol{P}_{\text{inp}} - \vec{\mu}_{\boldsymbol{P}_{\text{cum}}})/\mu\text{m}$	$(\boldsymbol{P}_{\text{inp}} - \vec{\mu}_{\boldsymbol{P}_{\text{glo}}})/\mu\text{m}$	$\vec{u}_{\boldsymbol{P}_{\text{cum}}}/\mu\text{m}$	$\vec{u}_{\boldsymbol{P}_{\text{glo}}}/\mu\text{m}$
4	3.93×10^{-05}	3.26×10^{-10}	4.03×10^{-05}	8.02×10^{-12}
5	1.54	-0.01	0.49	0.45
6	9.48×10^{-05}	8.42×10^{-10}	9.73×10^{-05}	7.23×10^{-12}
12	5.60×10^{-05}	2.47×10^{-10}	5.68×10^{-05}	1.24×10^{-12}
13	-0.11	-4.90×10^{-05}	0.14	0.21×10^{-02}
14	0.01×10^{-02}	5.97×10^{-10}	0.01×10^{-02}	2.70×10^{-12}
24	0.01×10^{-02}	2.41×10^{-10}	0.012×10^{-02}	1.08×10^{-10}
25	-0.03	-2.98×10^{-07}	0.10	1.34×10^{-05}
26	0.03×10^{-02}	5.81×10^{-10}	0.03×10^{-02}	2.61×10^{-10}

of a normal distributed random variable. Thus, equation (14) describes the translation of the uncertainty in the Zernike coefficient vectors to the topography uncertainty. Details of this notation are introduced in [11].

The results of the virtual experiment are depicted in table 1, figure 5 and table 2 for the aspherical and spherical specimen respectively. Since, the normally distributed radial displacement errors $u_{r,k}$ cause a normally distributed topography deviation in the stitched topography as demonstrated

in [11], they do not directly contribute to the systematic deviations in the mean Zernike coefficient vectors $\vec{\mu}_{\boldsymbol{P}_{\text{cum}}}$, $\vec{\mu}_{\boldsymbol{P}_{\text{glo}}}$.

4.1. Systematic deviations in the simulation

Figure 5(a) shows the systematic deviations in the stitched topography of the asphere. The deviations in the mean Zernike coefficient vectors $\vec{\mu}_{\boldsymbol{P}_{\text{cum}}}$, $\vec{\mu}_{\boldsymbol{P}_{\text{glo}}}$ are listed in the second and third column of tables 1 and 2. The results show, that the

systematic topography errors mainly affect the Zernike coefficients associated with defocus Z_0^2, $i = 5$ and spherical aberration Z_0^4, $i = 13$ and are much bigger for the cumulative stitching than for the global stitching approach. In case of the global stitching, the systematic deviation is most probably caused by the offset and tilt correction between the subapertures employing the first order Cartesian polynomials to fit a plane into each subaperture compensating their relative tilt to each other. In case of a sphere with constant curvature, the realignment of the subapertures by adding the first order polynomials in radial direction may yield an ideal result. However, if the topography includes an aspherical component and the curvature is dependent on the radial position, the fitted planes and offsets, which minimize the optimization problem described in section 3.2, do not perfectly represent the actual tilt of the subapertures at each radial position. A mismatch in the restored tilt and offset of the subapertures influences the radius of the retrieved global topography and thus, the defocus term of the Zernike coefficients. Additionally, the difference between the tilt of the Cartesian best fit polynomials and the actual slope of the topography causes a spherical aberration. This explanation is supported by the provided measurement results, since the systematic error in case of the global stitching is much bigger for the aspherical specimen than for the spherical specimen.

In case of the cumulative stitching this effect should not occur. The local subaperture tilt is calculated based on the information of the overlapping regions. If no measurement or alignment errors occur, any differences in those regions may be described by a tilt and an offset. However, in case of the cumulative stitching the tilt and offset of the subapertures to each other is restored iteratively and each deviation in the offset and local slope of the subaperture k affects the offset and slope restored for subaperture $k + 1$. The radial displacement error is normally distributed for each subaperture with the standard uncertainty $u_{r,k}$. Since the deviations in each iterative stitching step are inherited to the next, the effects of the radial displacement errors derived from multiple normal distributions with different standard deviation add up in the stitching process, which influences the mean value of the distribution and probably causes the systematic deviation in the mean values of the Zernike polynomials associated with the cumulative stitching. Besides that, the deviations in the retrieved offset and tilt of the subapertures affect the global topography in the same way as described for the global stitching and predominantly influence the defocus and spherical aberration term.

4.2. Statistical deviations in the simulation

The normally distributed topography deviations, represented by the combined uncertainty $u_{W,\text{cum}}$, $u_{W,\text{glob}}$ are depicted in figure 5(b) for the aspherical specimen. These deviations are caused by the normally distributed radial displacement errors $e_{r,k}$ applied in the virtual experiment. They affect the global and cumulative stitching in a similar manner, since they cause misalignments of the radial intervals $r_k + e_{r,k} = [r_{k0}, r_{k1}] + e_{r,k}$ and thus, an erroneous assignment of the subaperture

Table 3. Spherical specimen: mean values and standard uncertainty of the estimated radius of curvature $R_{\text{sph}} = 150$ mm, employing the topography results retrieved from cumulative and global stitching respectively.

$\mu_{R_{\text{sph,cum}}}/\text{mm}$	$\mu_{R_{\text{sph,glo}}}/\text{mm}$	$u_{R_{\text{sph,cum}}}/\text{mm}$	$u_{R_{\text{sph,glo}}}/\text{mm}$
149.78	150.00	0.14	0.13

topographies with respect to their radial coordinates. As a consequence, the offset and tilt of the correction planes used to realign the subapertures in the global coordinate system are calculated with a set of erroneous supporting points and do not match the actual tilt and offset of the subaperture. The erroneously restored radius of the topography influences the defocus term of the Zernike coefficients. The retrieved tilts of the subapertures are different for each of the subapertures and thus do not represent a perfect sphere, but an asphere with varying curvature, which influences the spherical aberration term. Since the simulation considers rotationally invariant specimens (the topography $\tilde{W}(r, \theta)$ does not change if it is rotated around the global z-axis) the asphericity caused by the erroneous tilt compensation is also rotationally invariant. Therefore, it is mainly represented by the rotationally invariant Zernike polynomials $Z_0^{(2\xi)} \forall \xi \in \mathbb{N}_{>0}$. For $L = 36$ Zernike coefficients these are Z_0^2, $i = 5$, Z_0^4, $i = 13$ and $Z_0^6, i = 25$. The influence of the lateral displacement errors on the measured topography increases with a stronger curvature of the surface, which is represented in the results of the virtual experiment comparing the combined uncertainties $u_{W,\text{cum}}$, $u_{W,\text{glo}}$ for the spherical object with base radius $R_{\text{sph}} = 150$ mm and the aspherical object with base radius $R_{\text{asph}} = 40.6193$ mm.

The simulation results presented in figure 5, tables 1 and 2 demonstrate the statistical topography deviations, based on the model of the normally distributed radial displacement errors $e_{r,k}$ and described by the combined uncertainties $u_{W,\text{cum}}$ and $u_{W,\text{glo}}$, to be in the single digit μm range. Based on the retrieved topography described by the Zernike coefficient vectors $\boldsymbol{P}_{\text{cum}}$ and $\boldsymbol{P}_{\text{glo}}$ on the unit circle, an estimate of the curvature R of the specimen can be calculated by the radius of a BFS that is fitted into the measured data point cloud $W(r, \theta)$. For the fitting, the radial position r is scaled from the unit circle to the assumed field of view $r \in [0, D_{\text{FOV}}/2]$. However, in the measurement the actual field of view depends on the accumulated radial displacement errors $\tilde{D}_{\text{FOV}} = D_{\text{FOV}} + 2 \sum_{k=1}^{K} e_{r,k}$. Thus, the measured topography $W(r, \theta)$, which already contains form deviations caused by the radial displacement errors is assigned to the assumed field of view D_{FOV}, although considering the unknown radial displacement errors it is actually measured on $\tilde{D}_{\text{FOV}}$. Thus, when fitting the BFS, the topography values as well as the lateral coordinates are affected by the radial displacement errors. Table 3 shows the mean value and standard deviation of the radius of curvature estimated from the topography simulation results of the spherical specimen. In accordance to the topography deviations, the estimates of the radius of curvature in table 3 show a systematic deviation when employing the
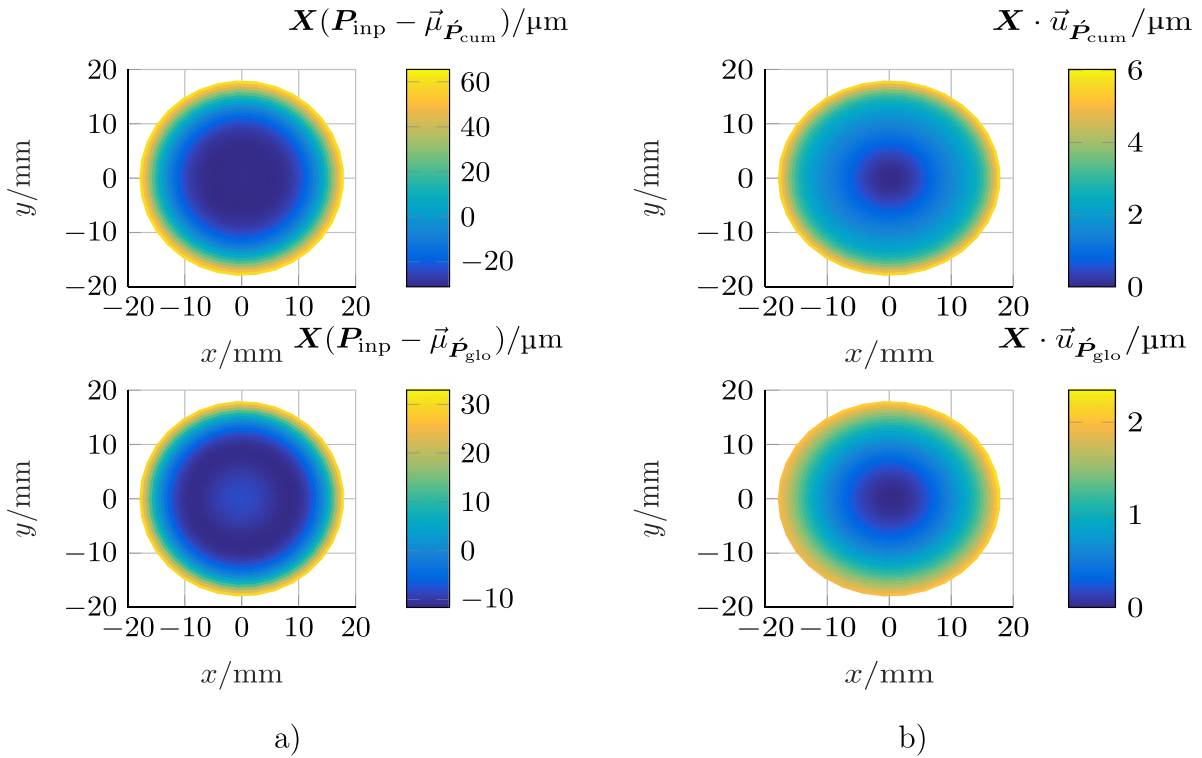
Figure 6. Aspherical specimen ($K = 21$, $\alpha_K \approx 26.8°$): (a) difference between the mean value of the retrieved output topographies, described by the Zernike coefficient vectors as given in equations (5) and (10), and the fiducial input topography represented by the coefficients of $\boldsymbol{P}_{\mathrm{inp}}$. This difference indicates systematic errors. (b) Estimates of the experimental standard uncertainty $u_{W,\mathrm{cum}}$ and $u_{W,\mathrm{glo}}$ in dependence of the lateral position in the field of view.

topography results from the cumulative stitching and the standard deviation is similar for both algorithms. However, due to the influence of the erroneous estimate of the diameter D_{FOV} when fitting the topography into a BSF, the uncertainty in the estimated radius of curvature significantly increased.

5. Comparison of the simulation to experimental results

The spherical and aspherical specimen described in section 4 are measured with the tiltable, interferometric line sensor introduced in section 2. The locally unwrapped annular subapertures $w(r_k, \theta)$ are stitched together employing the algorithms in section 3. The topography results described by the Zernike coefficient vectors $\boldsymbol{P}_{\mathrm{cum}}$, $\boldsymbol{P}_{\mathrm{glo}}$ are compared to the simulated coefficients to validate the feasibility of the virtual experiment that estimates the influence of normally distributed lateral displacement errors on the experimental topography deviations. Figure 6 and table 4 show the measurement results of the aspherical specimen, which are compared to the simulation of the aspherical specimen in figure 5 and table 1. Due to the high slope angles occurring on the surface of the aspherical specimen the field of view on a single subaperture is reduced to $|r_{k1} - r_{k0}|_\perp \approx 1.25$ mm. This is required to yield resolvable fringes and feasible modulation depth in the interferograms recorded with the filtered LED illumination of $\lambda \approx 532$ nm and FWHM ≈ 10 nm. Although

Table 4. Aspherical specimen ($K = 21$, $\alpha_K \approx 26.8°$): difference of the mean value of the output polynomials $\vec{\mu}_{\boldsymbol{\acute{P}}_{\mathrm{cum}}}$, $\vec{\mu}_{\boldsymbol{\acute{P}}_{\mathrm{glo}}}$ and the fiducial input $\boldsymbol{P}_{\mathrm{inp}}$. Standard deviation of the Zernike coefficient vectors $\vec{u}_{\boldsymbol{\acute{P}}_{\mathrm{cum}}}$ and $\vec{u}_{\boldsymbol{\acute{P}}_{\mathrm{glo}}}$ visualized in figure 6. The mean values and standard deviation are based on a set of $N = 6$ measurements of the aspherical specimen. The coefficients i are selected to show the main contributing coefficients $i = 5, 13, 25$ and their neighboring coefficients for comparison.

i	$(\boldsymbol{P}_{\mathrm{inp}} - \vec{\mu}_{\boldsymbol{\acute{P}}_{\mathrm{cum}}})/\mu\mathrm{m}$	$(\boldsymbol{P}_{\mathrm{inp}} - \vec{\mu}_{\boldsymbol{\acute{P}}_{\mathrm{glo}}})/\mu\mathrm{m}$	$\vec{u}_{\boldsymbol{\acute{P}}_{\mathrm{cum}}}/\mu\mathrm{m}$	$\vec{u}_{\boldsymbol{\acute{P}}_{\mathrm{glo}}}/\mu\mathrm{m}$
4	0.06	0.04	0.47×10^{-02}	0.15×10^{-02}
5	-48.70	-20.11	2.44	1.02
6	0.04	-0.49×10^{-02}	0.45×10^{-02}	0.84×10^{-02}
12	-0.02	-0.02	0.10×10^{-02}	0.09×10^{-02}
13	-17.42	-12.19	0.55	0.05
14	-0.02	-0.02	0.13×10^{-02}	0.33×10^{-02}
24	0.01	0.57×10^{-02}	0.15×10^{-02}	0.17×10^{-02}
25	0.73	-0.17	0.50	0.035
26	0.01	0.31×10^{-02}	0.20×10^{-02}	0.32×10^{-02}

the width of the annular subapertures in the simulations are chosen according to the line width employed in the experiment the total number of subaperture measurements in the simulation and the measurement are not identical. The aspherical object is simulated employing $K = 19$ subapertures and measured in $K = 21$ subapertures, while the spherical specimen is simulated employing $K = 11$ subapertures
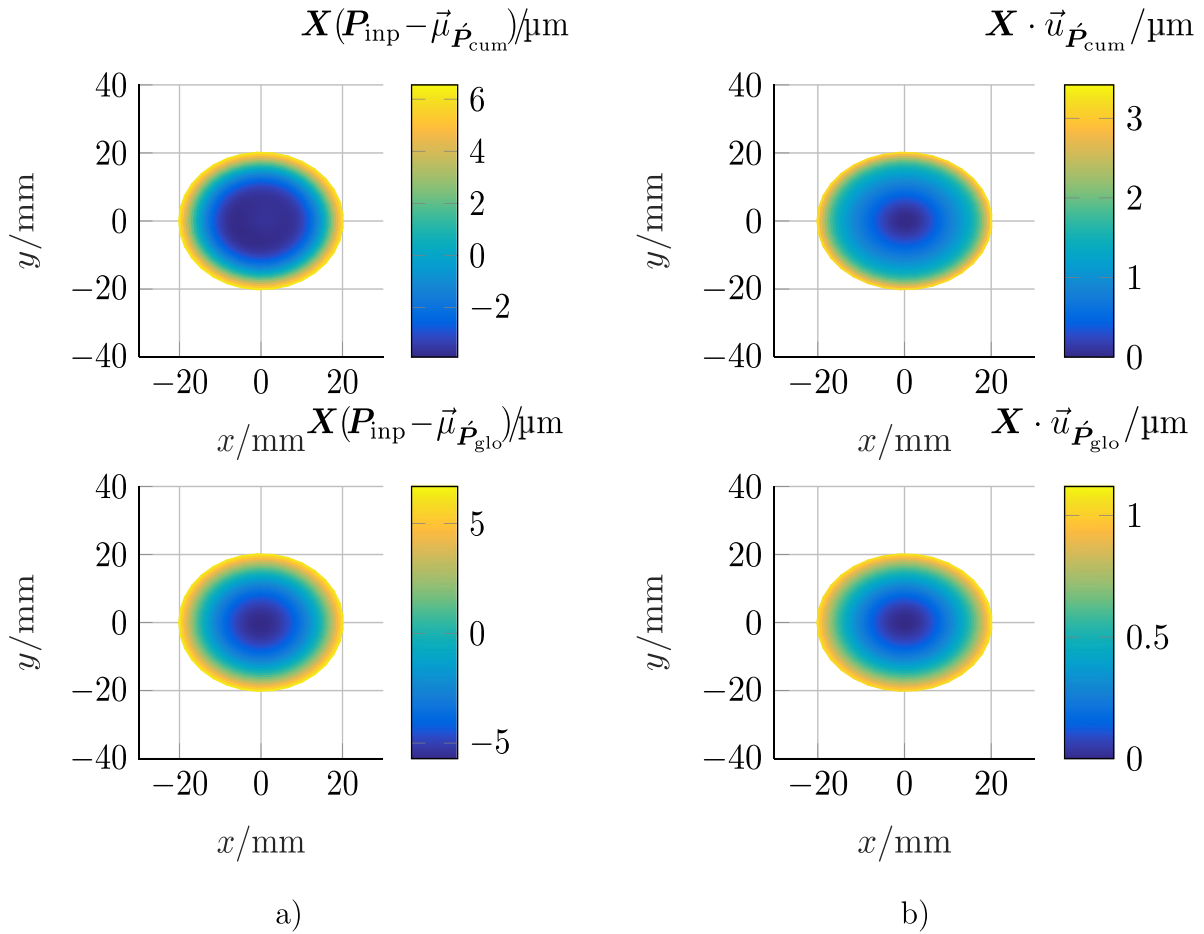
Figure 7. (a) Spherical specimen ($K = 10$, $\alpha_K \approx 6.5°$): difference between the mean value of the retrieved output topographies, described by the Zernike coefficient vectors as given in equations (5) and (10), and the fiducial input topography represented by the coefficients of $\boldsymbol{P}_{inp}$. This difference indicates systematic errors. (b) Spherical specimen: estimates of the experimental standard uncertainty $u_{W,cum}$ and $u_{W,glo}$ in dependence of the lateral position in the field of view.

and measured in $K = 10$ subapertures. The difference in the number of employed subapertures originates from the difference in the overlapping areas chosen in the simulation and the experiment, which also cause a difference in the absolute field of view covered by the K-subapertures. The simulation employs an algorithm to adapt the step width along the radial direction in dependence of the surface slope. The experiment is not yet fully automated, and the step width may need to be adjusted manually between subaperture measurements. The position of the linear and rotation axis is recorded and employed to assign the lateral coordinates of the measured subaperture. Therefore, the overlapping regions differ between the experiment and simulation. However, measurement and simulation cover a similar field of view. For comparison the Zernike coefficients describing the surface form of the simulated and measured topography are evaluated at the same points. Considering equation (13) it is apparent, that the model of the lateral displacement errors has no immediate dependence on the absolute number of subapertures. Yet the difference in the number of subapertures K, the maximum tilting angle α_K and the width and position of the overlapping areas influences the simulation results and contributes to the differences between experiment and model.

5.1. Systematic deviations

Figure 6(a) shows the difference between the mean value of the retrieved output topographies and the design function of the asphere and therefore indicates systematic deviations. Comparing the figures 5(a) and 6(a), shows a significant influence of systematic deviations in the output topography of the measurement, while the simulated topography shows only a small systematic deviation for the cumulative stitching and almost no systematic deviation for the global stitching approach. The virtual experiment in section 4 does not consider systematic deviations of the setup, which explains the above observation. There are multiple sources of the systematic deviations in the experiment. The dominant systematic effect arises from the tilting error e_α, depicted in figure 1. For the virtual experiment the tilting error e_α is expected to be normally distributed and causes a normally distributed lateral displacement error on the local subapertures. However, the backlash of the rotary axis causes a systematic component of e_α. When the interferometer is moved to the next subaperture by traveling the distance $x_{it,k}$ the assumed tilt angle α_k is employed to calculate the next radial position. If the actual tilt angle is $\alpha_k + e_\alpha$ the deviation e_α causes an erroneous assertion

a)

b)
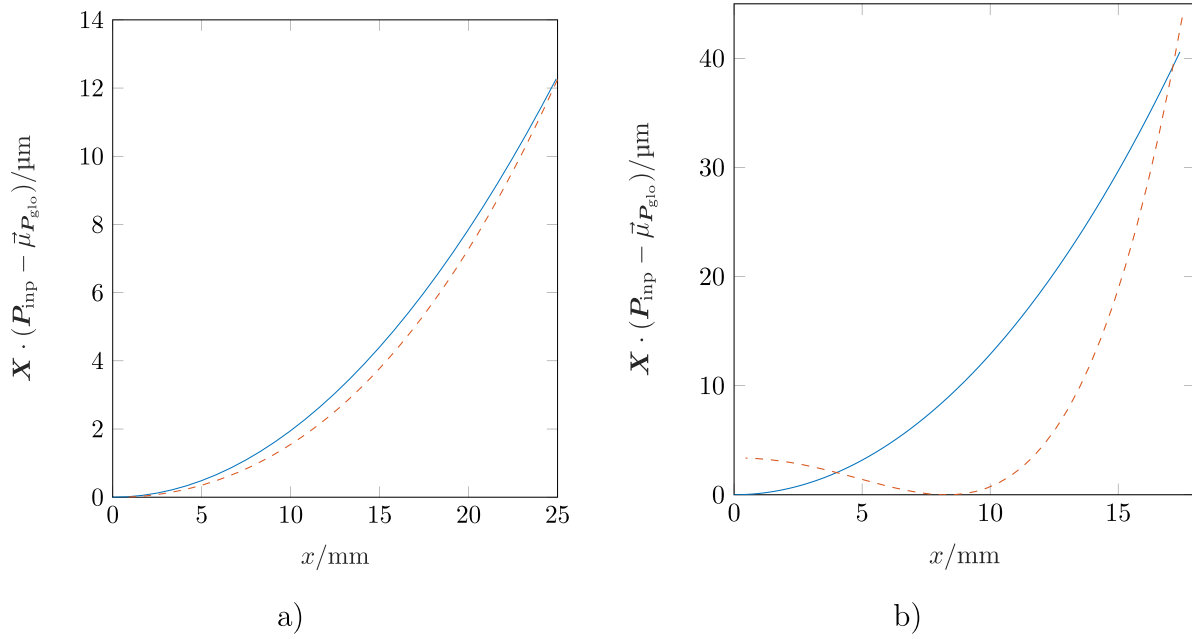
Figure 8. (a) Spherical specimen ($K = 11$, $\alpha_K \approx 8.7°$, $e_{\alpha,\text{sys}} = 4.45''$, $L_{\text{ref}} + L_{\text{rot}} = 126$ mm, $e_{r,\text{sys}}(K) = 26.4$ µm): Sectional view of the systematic deviations of the spherical specimen along the *x*-axis. Simulation with systematic displacement error (blue line), measurement results according to figure 7 (red dashed line). (b) Aspherical specimen ($K = 19$, $\alpha_K \approx 23.6°$, $e_{\alpha,\text{sys}} = 2.2''$, $L_{\text{ref}} + L_{\text{rot}} = 101$ mm, $e_{r,\text{sys}}(K) = 18.7$ µm): Sectional view of the systematic deviations of the aspherical specimen along the *x*-axis. Simulation with systematic displacement error (blue line), measurement results according to figure 6 (red dashed line).

of the next radial interval, which accumulates for each subaperture. The systematic deviation in the radial position on the *k*th subaperture may be estimated as

$$e_{r,\text{sys}}(k) = (k-1)(L_{\text{ref}} + L_{\text{rot}})e_{\alpha,\text{sys}}(k). \quad (15)$$

The local topography $w(r_k, \theta)$ is measured with an additional tilt, as depicted in figure 1 (pos. $k+1$) and thus has a different form, which influences the global topography result of the stitching algorithm. These tilting errors may be understood as a distortion of the input wavefront. In case of an ideally spherical measurement object and perfect perpendicular alignment of the interferometer to the surface on each subaperture, the local subapertures would be recorded as depicted in figure 2(a). Each subaperture would yield a symmetric pole cap and the incoming wavefronts would be aligned perpendicular to the spherical specimen along the spherical motion trajectory of the interferometer. However, if a tilting error e_α occurs, as depicted in figure 1 (pos. $k+1$), the incoming wavefront has a different angle and the considered section of the spherical specimen is measured as an aspherical form. The interferometer can not distinguish between the change in the input wavefront and an actual surface form change. If the topography stitching is performed, the erroneous measured surface form of the subaperture with the tilting error is employed, influencing the global topography result. Figure 8 visualizes the influence of a systematic tilting error $e_{\alpha,\text{sys}}$ according to equation (15) in the simulation of the spherical and aspherical specimen in comparison to the systematic deviation in the experiment for the global stitching algorithm. For comparison the Zernike polynomials of the simulated ($\boldsymbol{P}_{\text{inp}} - \vec{\mu}_{\boldsymbol{P}_{\text{glo}}}$) and measured ($\boldsymbol{P}_{\text{inp}} - \vec{\mu}_{\hat{\boldsymbol{P}}_{\text{glo}}}$) systematic deviations are evaluated in a field of view

of $D_{\text{FOV}} = 50$ mm for the sphere and $D_{\text{FOV}} = 35$ mm for the asphere and their offsets are aligned. As outlined in section 4 the radial displacement error e_r affects the rotationally invariant Zernike polynomials $Z_0^{(2\xi)} \forall \xi \in \mathbb{N}_{>0}$. The systematic displacement error $e_{r,\text{sys}}$ mainly affects the defocus term $i = 5$. Figure 8(a) shows, that in case of a spherical specimen the systematic deviations in the experiment may be sufficiently modeled by a systematic displacement error. However, as depicted in figure 8(b) the systematic deviations in case of the aspherical specimen contains relevant Zernike polynomials, which may not be modeled by a systematic displacement error, but would require the simulation of the original interferometric data to include the impact of the tilting error on the recorded interferogram. Another source of systematic deviations in the experimental setup are changes in the calibrated absolute distance $L_{\text{ref}} + L_{\text{rot}}$, due to mechanical settling or thermal influences. This results in a systematic misalignment of the interferometer, since the radial intervals and tilt angles are calculated employing an erroneous calibration distance. To reduce this effect, the calibration routine can be performed immediately before the start of a measurement series. The results presented in figure 8, demonstrate, that the systematic deviations occurring during measurement may not be modeled by a systematic displacement error alone.

5.2. Statistical deviations

The statistical deviations of the measured asphere topography are depicted in figure 6(b). Comparing the results of the measurement to the simulated topography in figure 5(b), shows a good agreement in the form, with a low uncertainty

Table 5. Spherical specimen ($K = 10$, $\alpha_K \approx 6.5°$): difference of the mean value of the output polynomials $\vec{\mu}_{\hat{P}_{\text{cum}}}$, $\vec{\mu}_{\hat{P}_{\text{glo}}}$ and the fiducial input P_{inp}. Standard deviation of the Zernike coefficient vectors $\vec{u}_{\hat{P}_{\text{cum}}}$ and $\vec{u}_{\hat{P}_{\text{glo}}}$ visualized in figure 7. The mean values and standard deviation are based on a set of $N = 20$ measurements of the spherical specimen. The coefficients i are selected to show the main contributing coefficients $i = 5, 13, 25$ and their neighboring coefficients for comparison.

i	$(P_{\text{inp}} - \vec{\mu}_{\hat{P}_{\text{cum}}})/\mu m$	$(P_{\text{inp}} - \vec{\mu}_{\hat{P}_{\text{glo}}})/\mu m$	$\vec{u}_{\hat{P}_{\text{cum}}}/\mu m$	$\vec{u}_{\hat{P}_{\text{glo}}}/\mu m$
4	0.95×10^{-02}	0.73×10^{-02}	0.06×10^{-02}	0.10×10^{-02}
5	-5.59	-6.18	1.45	0.52
6	0.06	0.05	0.12×10^{-02}	0.19×10^{-02}
12	-0.76×10^{-02}	-0.75×10^{-02}	0.11×10^{-02}	0.11×10^{-02}
13	-1.38	-0.44	0.28	0.03
14	-0.01	-0.01	0.09×10^{-02}	0.10×10^{-02}
24	0.82×10^{-02}	0.70×10^{-02}	0.11×10^{-02}	0.10×10^{-02}
25	0.52	0.03	0.23	0.02
26	0.90×10^{-02}	0.73×10^{-02}	0.15×10^{-02}	0.12×10^{-02}

Table 6. Spherical specimen: mean values and standard uncertainty of the measured radius of curvature $R_{\text{sph}} = 150\,\text{mm}$ employing the topography results retrieved from cumulative and global stitching respectively. The mean values and standard deviation are based on a set of $N = 20$ measurements of the spherical specimen.

$\mu_{R_{\text{sph,cum}}}/\text{mm}$	$\mu_{R_{\text{sph,glo}}}/\text{mm}$	$u_{R_{\text{sph,cum}}}/\text{mm}$	$u_{R_{\text{sph,glo}}}/\text{mm}$
151.07	151.32	0.35	0.11

on the inner subapertures, which increases toward higher subapertures. Figure 7 and table 5 show the experimental results of $N = 20$ repetition measurements of the spherical specimen, which are compared to the simulated result in table 2. For a detailed comparison of the topography's combined uncertainty $u_{W,\text{glo}}$ in dependence of the Zernike coefficients uncertainty $\vec{u}_{P_{\text{glo}}}$ as given in equation (14), the figures 9 and 11 are employed. Figure 9 shows the development of the combined uncertainty along the x-axis for the simulated and measured results. In case of the spherical specimen, the simulated uncertainty $X \cdot \vec{u}_{P_{\text{glo}}}$ shows a good agreement with the measured uncertainty $X \cdot \vec{u}_{P'_{\text{glo}}}$. For the aspherical specimen, the simulated uncertainty is considerably higher than the measured uncertainty. The aspherical measurement employed a different algorithm to align the sensor in the balanced path length condition and perpendicular to the specimen, which may explain the lower uncertainty in the measurement. The key observation in figure 9(b) is, that to model the uncertainty of the topography measurement for the aspherical specimen the lateral displacement uncertainty u_r has to be adapted. In [11], it is demonstrated by simulations, that the radial displacement errors e_r transfers almost linear through the stitching procedures. Therefore, the easiest method to adapt the model is to scale u_r according to the ratio $\max(X \cdot \vec{u}_{P'_{\text{glo}}})/\max(X \cdot \vec{u}_{P_{\text{glo}}})$. The relative deviation, between the simulation result for the scaled displacement uncertainty u_r will than be almost equal to the relative deviation of the normalized combined uncertainties in figure 11. This is demonstrated comparing the combined uncertainty of a simulation with scaled radial displacement error to the measured uncertainty of the aspherical specimen in figure 10. The differences, between the simulation results in figures 10(b) and 11 (b) are caused by the independent normal distributions of the displacement error in the virtual experiments. The distribution of the normalized combined uncertainties of the simulation and measurements is depicted in figures 11(a) and (b) for the spherical and aspherical specimen respectively. The relative deviation

of the normalized combined uncertainties in the lower part of figure 11 shows the part of the deviations in the experimental measurement, which are not covered by the scaled model of the radial displacement errors. Since the radial displacement errors only affect the rotationally invariant Zernike coefficients $i = 5, 13, 25$, they are unfit to model optical aberrations or other influences, which may employ Zernike coefficients of arbitrary order. Therefore, the relative deviation of the normalized combined uncertainty of the simulation and measurement expresses the portion of the combined measurement uncertainty, which can not be modeled by displacement errors. In conclusion, for the spherical specimen $\approx 94\%$ and for the aspherical specimen $\approx 90\%$ of the statistical topography deviations may be modeled as radial displacement errors. If a feasible model of the radial displacement uncertainty u_r is identified it can be scaled with the coverage factor k_p, resulting in an estimate of the expanded uncertainty $U_{W,\text{glo}} \approx k_p X \cdot \vec{u}_{P_{\text{glo}}}$. However, the scaling of the combined uncertainty may not be employed for the results of the cumulative stitching algorithm, since its results are influenced by the systematic deviations.

The statistical deviations of the Zernike coefficients for the spherical object are smaller than for the aspherical specimen. This may be explained by the mild slope angle of the spherical object in comparison to the asphere. As described in equation (13), the radial uncertainty increases with the absolute tilt angle α_k. In case of the spherical specimen the highest tilt angle is $\alpha_K \approx 6.5°$ and the field of view is recorded in $K = 10$ subapertures. In case of the aspherical specimen the highest tilt angle is $\alpha_K \approx 26.8°$ and the field of view is recorded in $K = 21$ subapertures employing a smaller number of camera pixels to yield resolvable fringes and stay inside the coherence length within each subaperture. Thus, the influence of the tilting errors is expected to be higher in case of the aspherical specimen. For both specimens, the dominant Zernike coefficients belong to the rotationally invariant Zernike polynomials Z_0^2, $i = 5$, Z_0^4, $i = 13$ and $Z_0^6, i = 25$ as predicted by the simulation and in accordance to the expected rotationally invariant deviations caused by the radial displacement errors. However, the dominant Zernike coefficients are much sharper distinguished in the simulation results. For the experiment in tables 4 and 5 the dominant coefficients $i = 5$, 13, 25 are only a factor 10 to 100 bigger, than the other coefficients. This implies the influence of additional non rotationally invariant statistical deviations in the experiment, which are not included in the simulation and contribute to the deviation of the normalized combined uncertainties in figure 11.

A possible source may be local imperfections of the topography, scratches or dust particles. The simulation considers the surface of an ideal spherical or aspherical specimen with no
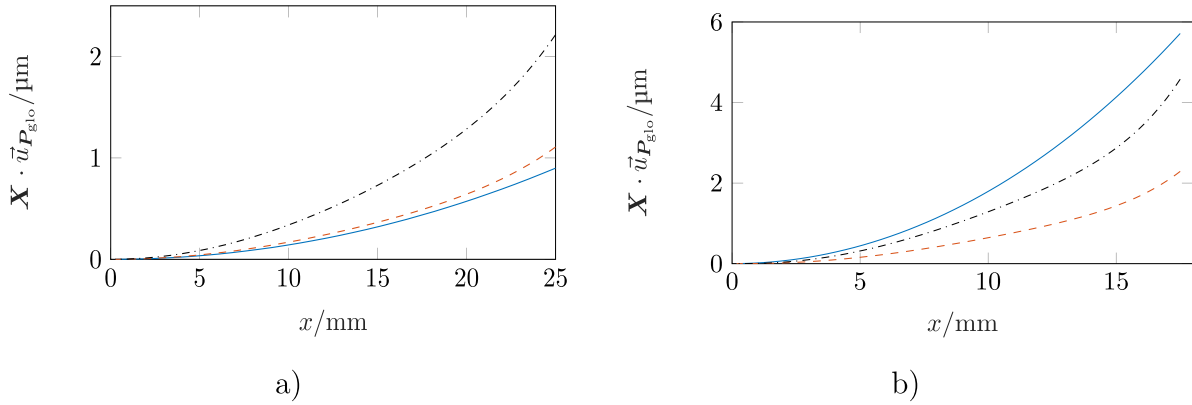
Figure 9. (a) Spherical specimen: sectional view of the combined uncertainty of the spherical specimen's topography along the *x*-axis. Simulation results according to table 2 (blue line), measurement results according to table 5 (red dashed line), 2σ-threshold of the measurement uncertainty (black dash-dotted line). (b) Aspherical specimen: sectional view of the combined uncertainty of the aspherical specimen's topography along the *x*-axis. Simulation results according to table 1 (blue line), measurement results according to table 4 (red dashed line), 2σ-threshold of the measurement uncertainty (black dash-dotted line).
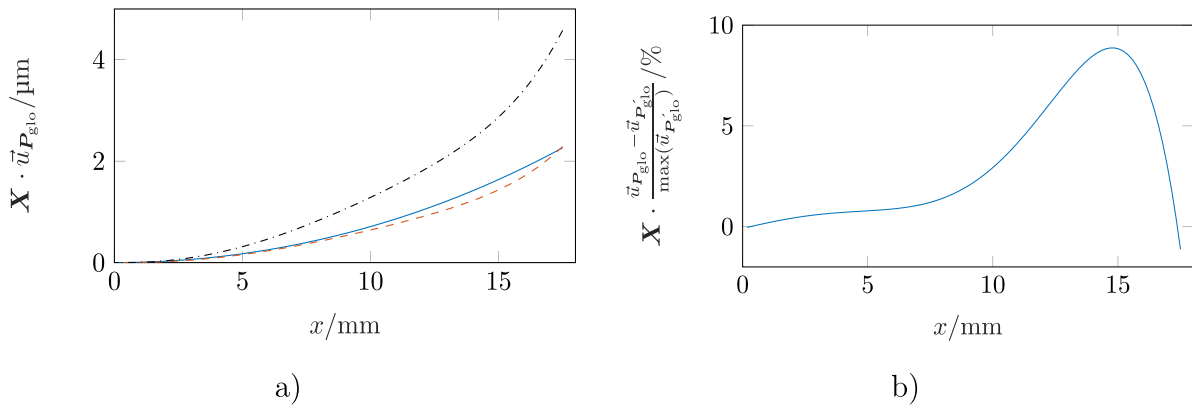
Figure 10. (a) Aspherical specimen: sectional view of the combined uncertainty of the aspherical specimen's topography along the *x*-axis. Simulation results with scaled u_r (blue line), measurement results according to table 4 (red dashed line), 2σ-threshold of the measurement uncertainty (black dash-dotted line). (b) Relative deviation between the combined uncertainty of the simulation results with scaled u_r and the combined uncertainty of the measurement.

defects. The actual specimens are likely to exhibit local surface defects, which will affect the Zernike polynomial fitting.

A comparison of tables 3 and 6 reveals that the restored radius of curvature for the spherical specimen shows a higher systematic deviation as predicted by the simulation, while the statistical deviations are estimated in the correct order of magnitude for the cumulative stitching and almost match for the global stitching. This is to be expected, since the radii of curvature are retrieved employing the Zernike coefficients describing the topography in a sphere fitting.

The comparison of the virtual experiment with the measurement data demonstrates that the simulation of radial displacement errors appears to be a suitable method to estimate an expanded measurement uncertainty of the topography measurement with the tiltable line scanning interferometer. Measurement and simulation are in good agreement for the global stitching and in comparison to the cumulative stitching it shows a smaller standard deviation in the experimental results. The simulation results show minor differences in the measurement uncertainty between global and cumulative stitching than the measurements. This indicates the occurrence

of experimental deviations influencing the cumulative stitching, which are not covered by the virtual experiment. Judging by the presented results, the global stitching algorithm yields better results than the cumulative stitching, when employed in the evaluation of the experimental data.

Comparing the systematic and statistical deviations of the topography retrieved by simulation and experiment to other ASSI based methods described in the introduction, the line scanning sensor shows a higher overall uncertainty with PV deviations in the µm regime. The possibility to assert an expanded uncertainty to the measurement results of the line scanning interferometer is non the less a promising feature and the introduced method to model the radial displacement uncertainty and propagate it through the stitching procedures employing a Monte Carlo simulation may be applicable to other ASSI setups with higher precision.

5.3. Outlook

In future work, the displacement error model may be expanded to cover systematic deviations and thus provide the means to
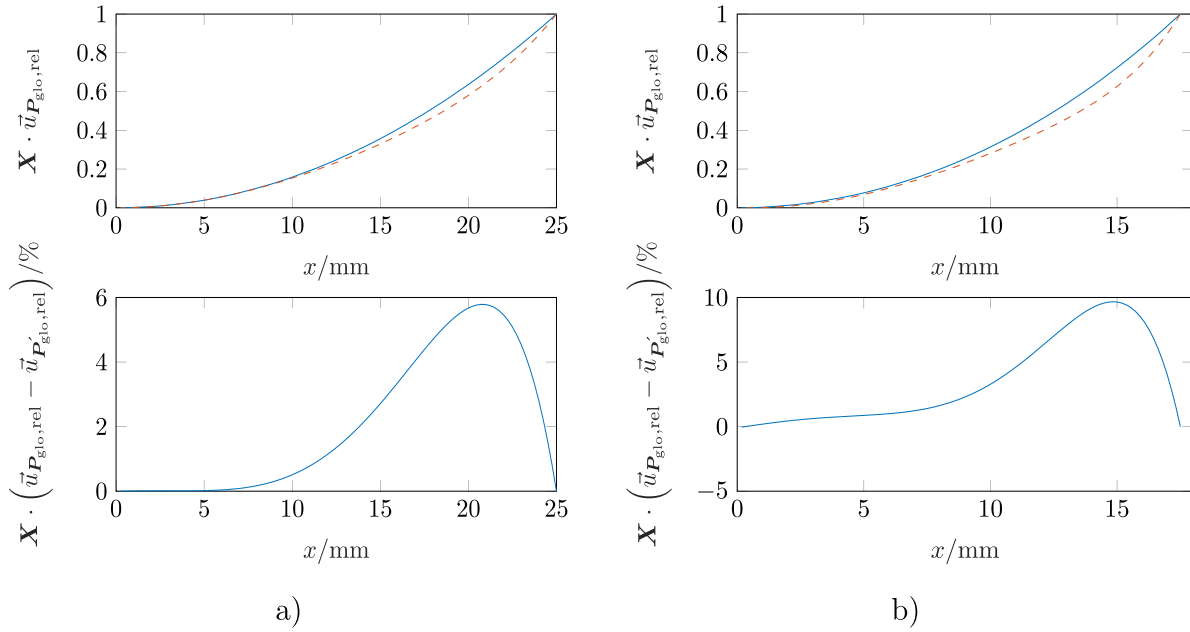
Figure 11. (a) Spherical specimen: sectional view of the normalized combined uncertainty of the spherical specimen's topography along the x-axis. Simulated normalized combined uncertainty $\vec{u}_{P_{\mathrm{glo}},\mathrm{rel}} = \frac{\vec{u}_{P_{\mathrm{glo}}}}{\max(\vec{u}_{P_{\mathrm{glo}}}) - \min(\vec{u}_{P_{\mathrm{glo}}})}$ (blue line) and measured normalized combined uncertainty $\vec{u}_{P'_{\mathrm{glo}},\mathrm{rel}} = \frac{\vec{u}_{P'_{\mathrm{glo}}}}{\max(\vec{u}_{P'_{\mathrm{glo}}}) - \min(\vec{u}_{P'_{\mathrm{glo}}})}$ (red dashed line). The lower plot shows the relative deviation between the normalized combined uncertainties. (b) Aspherical specimen: simulated normalized combined uncertainty (blue line) and measured normalized combined uncertainty (red dashed line). The lower plot shows the relative deviation between the normalized combined uncertainties.

correct the systematic measurement errors. To further improve the simulation results, the model of the statistical deviations may be expanded including electrical and thermal influences, which are currently not considered. Since present results demonstrate the compliance of the virtual experiments and measurements, further reduction of the uncertainty of the experimental procedure is desirable. A possibility to reduce the experimental measurement uncertainty is to decrease the angular uncertainty u_α, which has a strong influence on the radial displacement errors. This can be achieved by employing a high resolution encoder for the tilting axis B or the inclusion of an additional precise angle measurement of the *B*-axis.

6. Conclusion

To enable topography stitching of the subapertures recorded by a line scanning interferometric sensor for ASSI, a global stitching algorithm combining Cartesian- and Zernike polynomial fitting in a linear optimization problem is introduced.

A model of the normally distributed radial displacement errors occurring during an ASSI measurement employing a line scanning interferometer is proposed and their influence on the retrieved global topography results is demonstrated comparing experimental results and Monte-Carlo analysis. The uncertainty of the simulated topographies is compared to the standard deviation of experimental topography measurements. The comparison of simulated and experimental uncertainties shows that the modeling of radial displacement errors is a feasible approach to estimate the expanded uncertainty of the

topography measurements. Depending on the specimen's form approximately 90% of the measured statistical topography deviations are covered by the rotationally invariant Zernike polynomials Z_0^2, Z_0^4 and Z_0^6 and therefore may be modeled by the radial displacement errors. The experimental results indicate, that the global stitching algorithm yields a smaller measurement uncertainty than the cumulative stitching and should be employed for the procedure of topography measurements. The experimental results show systematic topography deviations, which are not included in the virtual experiment and in case of aspherical specimens may not be sufficiently modeled by a radial displacement error.

The comparison of the topography results of the virtual experiment to the experimental topography measurements summarized above, supports the theory stated in [11]. Topography deviations caused by normally distributed radial displacement errors may be suitably modeled as a normal distribution and thus, allow the estimation of an expanded uncertainty. The experimental demonstration of the predicted influence of statistical displacement errors on the topography, the successful implementation of the enhanced stitching algorithm and the detection of the strong systematic deviations in the measurement results, which are not covered by the model are the mayor advances presented in the contribution.

Acknowledgments

400/4-2) received from the Deutsche Forschungsgemeinschaft (DFG).

Data availability statement

ORCID iDs

Markus Schake https://orcid.org/0000-0002-9883-3494
Jörg Riebeling https://orcid.org/0000-0002-5997-8527
Peter Lehmann https://orcid.org/0000-0003-0051-5066
Gerd Ehret https://orcid.org/0000-0001-8432-4739

References

[1] Hou X, Wu F, Yang L, Wu S and Chen Q 2006 Full-aperture wavefront reconstruction from annular subaperture interferometric data by use of Zernike annular polynomials and a matrix method for testing large aspheric surfaces *Appl. Opt.* **45** 3442–55

[2] Hou X, Wu F, Yang L and Chen Q 2007 Experimental study on measurement of aspheric surface shape with complementary annular subaperture interferometric method *Opt. Express* **15** 12890–9

[3] Küchel M F 2009 Interferometric measurement of rotationally symmetric aspheric surfaces *Proc. SPIE* **7389** 738916

[4] Laubach S, Ehret G, Riebeling J and Lehmann P 2017 Combination of a fast white-light interferometer with a phase shifting interferometric line sensor for form measurements of precision components *Proc. SPIE* **10329** 103291D

[5] Liu Y M, Lawrence G N and Koliopoulos C L 1988 Subaperture testing of aspheres with annular zones *Appl. Opt.* **27** 4504–13

[6] Tricard M, Forbes G and Murphy P 2005 Subaperture metrology technologies extend capabilities in optics manufacturing *Proc. SPIE* **5965** 59650B

[7] Murphy P, Fleig J, Forbes G, Miladinovic D, DeVries G and O'Donohue S 2006 Subaperture stitching interferometry for testing mild aspheres *Proc. SPIE* **6293** 62930J

[8] Riebeling J, Ehret G and Lehmann P 2019 Optical form measurement system using a line-scan interferometer and distance measuring interferometers for run-out compensation of the rotational object stage *Proc. SPIE* **11056** 110562D

[9] Schake M and Ehret G 2020 Annular subaperture stitching interferometry with planar reference wavefront for measurement of spherical and aspherical surfaces *Proc. SPIE* **11523** 115230D

[10] Schake M and Ehret G 2020 Machine learning based fitting of zernike polynomials for ASSI *DGaO-Proc. 2020* vol 121 p A31

[11] Schake M, Riebeling J and Ehret G 2020 Form deviations caused by lateral displacement errors in annular subaperture stitching interferometry *Opt. Eng., Bellingham* **59** 1–17

[12] Wang X, Wang L, Yin L, Zhang B, Fan D and Zhang X 2007 Measurement of large aspheric surfaces by annular subaperture stitching interferometry *Chin. Opt. Lett.* **5** 645–7

[13] Wen Y, Cheng H, Tam H Y and Zhou D 2013 Modified stitching algorithm for annular subaperture stitching interferometry for aspheric surface *Appl. Opt.* **52** 5686–94

[14] Wen Y and Cheng H 2014 Measurement of aspheric surfaces using annular subaperture stitching interferometry based on an automatic positioning method: theory and application *Opt. Eng.* **53** 1–10

[15] Baer G, Schindler J, Pruss C, Siepmann J and Osten W 2014 Calibration of a non-null test interferometer for the measurement of aspheres and free-form surfaces *Opt. Express* **22** 31200–11

[16] Blobel G, Wiegmann A, Siepmann J and Schulz M 2016 Metrological multispherical freeform artifact *Opt. Eng., Bellingham* **55** 1–8

[17] Selberg L A 1992 Radius measurement by interferometry *Opt. Eng., Bellingham* **31** 1961–6

[18] Sommer D, Schulz M, Wiegmann A and Triefenbach N 2017 Erweiterte anwendungen bei der radiusmessung optischer komponenten *DGaO-Proc. 2020* (DGaO) 128 P28

[19] Schachtschneider R *et al* 2018 Interlaboratory comparison measurements of aspheres *Meas. Sci. Technol.* **29** 055010

[20] Knell H, Laubach S, Ehret G and Lehmann P 2014 Continuous measurement of optical surfaces using a line-scan interferometer with sinusoidal path length modulation *Opt. Express* **22** 29787–98

[21] Ibañez D R, Gómez-Pedrero J A, Alonso J and Quiroga J A 2016 Robust fitting of Zernike polynomials to noisy point clouds defined over connected domains of arbitrary shape *Opt. Express* **24** 5918–33

[22] Schulz M and Lehmann P 2013 Measurement of distance changes using a fibre-coupled common-path interferometer with mechanical path length modulatio *Meas. Sci. Technol.* **24** 065202

[23] Herráez M A, Burton D R, Lalor M J and Gdeisat M A 2002 Fast two-dimensional phase-unwrapping algorithm based on sorting by reliability following a noncontinuous path *Appl. Opt.* **41** 7437–44

[24] Lehmann P, Tereschenko S and Xie W 2016 Fundamental aspects of resolution and precision in vertical scanning white-light interferometry *Surf. Topography: Metrol. Prop.* **4** 024004

[25] Joint Committee for Guides in Metrology 2008 Evaluation of measurement data–guide to the expression of uncertainty in measurement *JCGM 100:2008, BIPM Joint Committee for Guides in Metrology, Paris* (available at: www.bipm.org/utils/common/documents/jcgm/JCGM_100_2008_E.pdf) (Accessed 27 April 2020)